UNIVERSITY OF COPENHAGEN

The Local Interstellar Environment of High-Redshift Star-Forming Galaxies Probed with Gamma-Ray Bursts
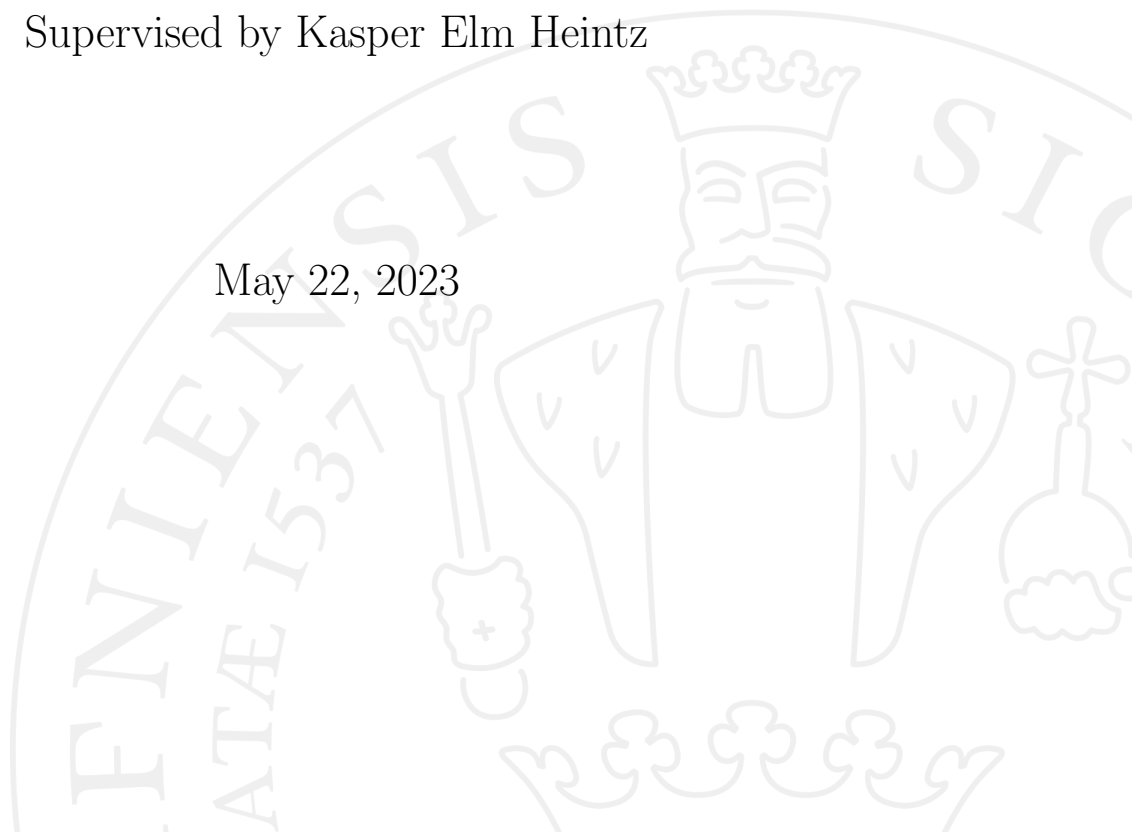
Master's Thesis

by

Lise Klungsøyr Nøland

Supervised by Kasper Elm Heintz

May 22, 2023

University of Copenhagen

Faculty: Science

Institute: Niels Bohr Institute

Author: Lise Klungsøyr Nøland

Title: The local interstellar environment of high-redshift star-forming galaxies probed with gamma-ray bursts

Supervisor: Kasper Elm Heintz

Submitted: May 22, 2023

Aknowledgements

I would like to thank my supervisor Dr. Kasper Heintz for all of his help and support throughout the duration of this thesis. Your knowledge and kindness made this experience both extremely educational and enjoyable. I would also like to thank my parents for their unwavering support.

Abstract

Studying the neutral hydrogen (HI) gas content in galaxies is essential for unraveling the processes which lead to their formation and evolution. Extensive HI-mapping of nearby galaxies has been performed using the 21-cm transition, but as this line is intrinsically faint, this approach is not feasible for galaxies at redshifts higher than $z \approx 0.4$. We adopt the method for obtaining the [CII]-to-HI conversion factor presented in Heintz et al. (2021), which can be used to infer the HI gas mass of individual star-forming galaxies at high redshifts through absorption line measurements from bright gamma-ray burst (GRB) afterglow spectra. This approach is extended in this thesis to also obtain [OI*]-to-HI and [OI**]-to-HI conversion factors for a sample of GRB afterglows observed with the VLT/UVES spectrograph. We find that [CII]-to-HI follows the expected anti-correlation with metallicity and that [OI*]-to-HI also shows such a dependence, although not as strong. This anti-correlation was not found for [OI**]-to-HI in our sample, which appeared to be independent of metallicity. Furthermore, we estimate the [CII*]-158 μm cooling rates to find the expected phase segregation in the interstellar medium to investigate whether our GRBs probe warm or cold neutral medium.

Contents

List of Figures

List of Tables

1 Introduction

1.1 Galaxy Formation

Modern galaxy formation theory is set within the standard Λ cold dark matter cosmological model (ΛCDM-model), which predicts a flat, expanding universe composed of dark energy, dark matter, baryonic matter, and electromagnetic radiation. Within this model, structure formation is believed to happen hierarchically through mergers of dark matter (DM) halos, in which the primordial gas can cool and condense to eventually form galaxies (Blumenthal et al., 1984).

The DM component has approximately zero pressure and must therefore undergo gravitational collapse, which causes density perturbations to grow and eventually virialize. This approximately stable state, where the self-gravity is balanced by the random motions of the particles comprised, is called a DM halo. The initial distribution of baryons in the primordial universe is nearly uniform, but to form stars and galaxies, they must cool and condense. The strong gravitational forces in the DM halos lead to the accretion of surrounding primordial gas, and the deep potential wells of the DM halos are therefore expected to be the sites where the accreted gas is concentrated to eventually form stars and galaxies.

At the highest redshifts ($z > 200$), the primordial gas, mainly composed of neutral hydrogen (Briggs, 2005), cannot cool through the usual atomic processes occurring in gas enriched with metals and gas that is hot enough for collisional ionization of hydrogen. At these redshifts, the temperature the gas reaches during the virialization is $T_{vir} < 10^4$ K, and the main coolant in these DM halos is the small fraction of molecular hydrogen (H_2) (Abel et al., 1997). This cooling and condensation of the gas by H_2 are believed to be the mechanisms behind the formation of the first generation of stars, Population III (Pop III) stars, which are expected to form at redshifts $z \gtrsim 20$ in DM minihalos with masses $10^5 - 10^6$ $M_\odot$ (Xu et al., 2013).

Considering the commonly accepted view that a galaxy must be able to host ongoing star formation, DM minihalos are not likely the hosts of the first galaxies, as the supernovae from the first stars may expel any dense gas from the halo and thereby prevent further star formation (Johnson, 2012). The first galaxies must therefore have formed later, in larger DM halos with

sufficient masses (around $10^7 - 10^8$ M$_\odot$) and potential wells deep enough to retain gas after earlier episodes of star formation (Kitayama & Yoshida, 2005; Read et al., 2006). Due to the first population of stars, the properties of the gas from which the first galaxies form have been altered. The strong radiation from the Pop III stars causes ionization in the primordial gas, as well as dissociation of molecules. Additionally, the Pop III stars, which end their lives in supernovae, enrich the gas with the first heavy elements.

The primordial gas collapsing into the DM halos is usually shock-heated to the virial temperature, which can be expressed as

$$T_{vir} \simeq 10^4 \text{ K } \left(\frac{M_{vir}}{5 \times 10^7 \text{ M}_\odot} \right)^{2/3} \left(\frac{1+z}{10} \right), \tag{1}$$

such that a halo with mass 5×10^7 M$_\odot$ at redshift $z \simeq 10$ is just massive enough to satisfy the atomic cooling criterion (Oh & Haiman, 2002). The higher temperature and mass allow the halo to cool via atomic hydrogen lines but also imply that gas that has been photoheated by hydrogen ionization can be retained (Dijkstra et al., 2004). This leads to higher rates of H$_2$ formation, as it is primarily formed through the reaction sequence

$$\begin{aligned} \text{e}^- + \text{H} &\rightarrow \text{H}^- + h\nu \\ \text{H}^- + \text{H} &\rightarrow \text{H}_2 + \text{e}^-, \end{aligned} \tag{2}$$

and hence more efficient cooling. With the decreasing temperature, the gas can no longer be supported by thermal pressure, making it settle in a disk (Fall & Efstathiou, 1980). In the hierarchical paradigm, these proto-galaxies containing the disks and stars merge, causing spherical structures to form. These evolve either in relative isolation to form spiral galaxies or through further mergers and interactions to form elliptical galaxies.

The first heavy elements are believed to have formed in the cores of the Pop III stars and were ejected into the primordial gas when they exploded as supernovae. The chemical enrichment and large release of mechanical energy alter the conditions of the gas from which the next generation of stars form. The halo hosting the primordial supernova will continue to grow until it reaches the point where its gravity is strong enough for the metal-enriched gas to collapse into it again, giving rise to the next generation of stars, Pop II stars. The halo mass required for this collapse corresponds to the ones large enough to host the first galaxies, M $\sim 5 \times 10^7$ M$_\odot$. The metals produced in

the stars are ejected by their supernovae and may also gather in dust clouds among the gas in the interstellar medium.

1.2 The Interstellar Medium

The interstellar medium (ISM) is composed of approximately 99% gas and around 1% dust. The fraction of neutral gas is dominated by neutral atomic hydrogen (HI) (Spitzer, 1998). Measuring the HI gas component of galaxies at high redshifts can reveal unique information about the evolution of the universe. It can provide information about how the first galaxies evolved, how the interstellar gas and intergalactic medium were affected by it, as well as how stars are formed within the galaxies.

1.2.1 The Neutral Gas Phase

Studying the ISM is essential for understanding the physical processes occurring inside a galaxy, as there is constant interaction between matter, momentum, and energy between the different phases of the ISM and the stars. The neutral gas of the ISM acts as the reservoir for the molecular clouds in which star formation occurs. The ISM also plays a vital role in the understanding of galaxy formation, as the intergalactic medium consists of metals from galactic outflows (Tumlinson et al., 2017). Additionally, galactic HI disks have been found to be very extended (Chung et al., 2009; Mihos et al., 2012), thus being affected by tidal interactions and mergers, which also connect the neutral atomic gas to galaxy formation.

Multiple studies have shown that the neutral gas of the ISM exists in pressure equilibrium and may thus be described as a two-phase medium (Field et al., 1969; Dickey et al., 1983; Wolfire et al., 1995; Dickey et al., 2000). The two main phases the ISM is typically divided into include the warm neutral medium (WNM), with typical temperature $\sim 10^4$ K, and the cold neutral medium (CNM), with typical temperature ~ 100 K. While photoelectric heating by dust grains is the dominant heating process of the neutral ISM, the cooling at temperatures $\lesssim 2000$ K is mainly a result of radiative cooling by [CII*]-158μm and [OI*]-63 μm fine-structure emission.

1.2.2 HI Gas Mass Measurements

The ideal probe of the HI gas content is the 21-cm line, arising from the hyperfine structure of the ground state of the hydrogen atom. Radio telescopes have enabled extensive HI-mapping of nearby galaxies from observations of the 21-cm transition (Zwaan et al., 2005; Martin et al., 2010). However, the sensitivity of radio telescopes is currently insufficient for the detection of the 21-cm line at high redshifts because the flux of the 21-cm emission signal is inversely proportional to the square of the distance to the source. Using the 21-cm line as a tracer for the total HI content has therefore only been attainable for redshifts up to z $\approx$ 0.4 (Fernández et al., 2016) with current radio telescopes, and an alternative approach is therefore needed to infer the HI gas content in more distant galaxies.

1.3 Gamma-Ray Bursts

A gamma-ray burst (GRB) is a sudden release of gamma rays with a duration of milliseconds to a few thousand seconds. Their peak luminosities have been estimated through measurements of their redshifts to be $\sim 10^{51} - 10^{53}$ erg s^{-1}, making GRBs the most luminous explosions in the universe after the Big Bang. The rapidly varying timescales of GRBs, which can be as short as a few milliseconds, suggest that the GRB progenitor must be on the stellar scale, with compact objects, such as black holes or neutron/quark stars, being the central engine. A longer and less luminous afterglow follows the initial explosion. GRBs are typically divided into two categories, long GRBS, with a typical duration of more than 2 seconds, and short GRBs, typically lasting less than 2 seconds.

This segregation suggests that long and short GRBs have different origins. There is substantial evidence suggesting that at least some long GRBs are associated with core-collapse supernovae of massive stars (M $\sim 20 - 30$ M$_\odot$) (Cobb, 2011; Hjorth & Bloom, 2011; Hjorth, 2013; Cano et al., 2017). The connection with supernovae first arose when SN1998bw was detected and found to be spatially and temporally consistent with GRB980425 (Galama et al., 1998). Observations of the afterglow spectra at optical wavelengths (optical transients) showing a rebrightening around 20-30 days after the initial explosion, which could be fit to the light curves of SN1998bw, further supported the connection (Zeh et al., 2005). It became even more convinc-

ing when characteristics of supernova spectra were observed in the afterglow spectrum of GRB030329 (Dado et al., 2003).
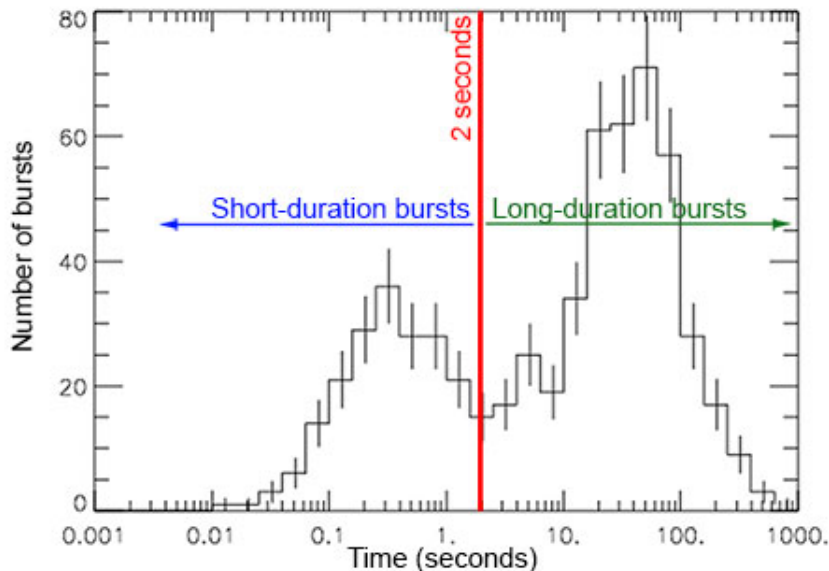
Figure 1: Time duration versus the number of GRBs observed by the BATS instrument on the Compton Gamma-Ray Telescope. Reprinted from nasa.gov (2013).

The origin of short GRBs is not as well established as for long GRBs, but the leading theory is that they originate from binary mergers of neutron stars forming a black hole (Rezzolla et al., 2011; Ruiz et al., 2016). This suggests that the host is likely an early-type galaxy. Similarly to the long GRBs, short GRBs also produce X-ray and optical afterglows and sometimes also X-ray flares (Barthelmy et al., 2005).

1.3.1 GRBs as Probes for High-Redshift Galaxies

Long GRBs have been shown through spectroscopic and photometric observations to primarily originate in faint, blue, low-mass, low-metallicity, star-forming galaxies (Floc'h et al., 2003; Prochaska et al., 2004; Christensen et al., 2004; Fynbo et al., 2005; Gorosabel et al., 2005; Savaglio et al., 2009). The supernova connection to the long GRBs indicates that they track the formation of massive stars and can be used to estimate star formation rates

13

at high redshifts where the application of other methods is limited. Furthermore, as some GRBs may come from the death of the first stars, they can carry valuable information about the epoch of re-ionization (Bromm & Loeb, 2006).

As GRBs likely come from the self-destruction of the progenitor system, it is extremely difficult to directly observe the system when the GRB is detected. However, the afterglow spectra of GRBs comprise a wide range of absorption lines that can be detected. Elements along the line of sight imprint absorption lines on the afterglow spectrum (Vreeswijk et al., 2007), and many absorption lines are observed at the redshift of the GRB. These lines originate from the gas reservoir of the host galaxy and therefore make it possible to infer the local neutral hydrogen column density and the metallicity of the host galaxy (Savaglio, 2006). Absorption lines of typical interest for characterizing the ISM have rest wavelengths in the ultraviolet and are redshifted in the optical at $z > 2$, making them easier to observe. A typical feature of GRB afterglow spectra is a strong damped Lyman alpha absorption line arising from a very high HI column density ($N > 10^{20.3}$) in the ISM. These systems are called Damped Lyman alpha (DLA) systems (Wolfe et al., 2005). The high HI column density enables the detection of species of low abundances and absorption lines from excited levels of atomic ground states. It also makes the derivation of metallicities easier, as most species will be in their neutral or singly ionized state at these high HI column densities, allowing metallicity derivation without ionization correction.

The ISM of galaxies at high redshifts is often characterized by observing intervening damped Lyman alpha systems along the line of sight to bright quasars (Wolfe et al., 2003; Noterdaeme et al., 2009). These may, however, be biased to low-density regions (Rauch et al., 2008) and do, therefore, not trace the regions of star formation. As long GRBs are produced from the death of massive stars, they are predicted to directly trace the regions where star formation occurs and are thus powerful probes of the high-density gas and molecular clouds (Campana et al., 2006; Prochaska et al., 2008). Figure 2 illustrates the assumed different sight lines of intervening QSO DLAs and GRB DLAs.
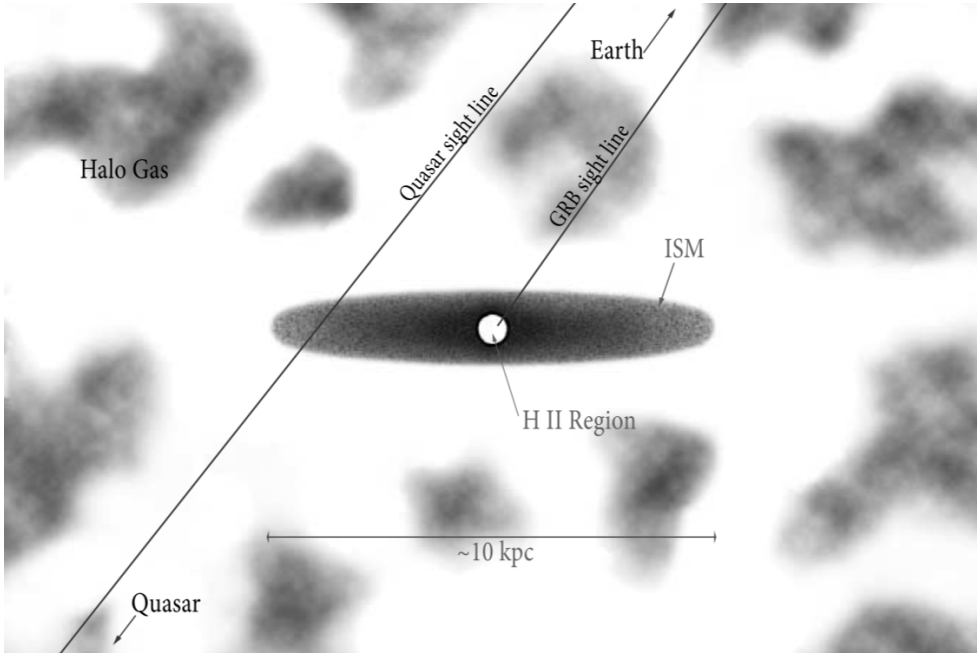
Figure 2: Illustration of the assumed different sight lines of damped Lyman alpha absorbers intersected by distant quasars (QSO DLAs) and GRB DLAs. Reprinted from Prochaska et al. (2007).

1.4 Motivation

Galaxy formation and evolution clearly play a central role in understanding the universe at high redshifts. With HI being the main component of the primordial gas collapsing into stars and galaxies and of the gas in the interstellar medium, knowing its interstellar abundance is key to understanding the properties of galaxies. As mentioned previously, HI mapping from 21-cm emission is currently unattainable at high redshifts, which motivates the use of GRBs probing high-redshift, star-forming galaxies. The absorption lines imprinted on the afterglow spectra of GRBs can reveal the local HI column density of the host galaxy. Metal absorption lines may also be imprinted on the afterglow spectra, and given that the main source of cooling in the ISM comes from [CII*]-158μm and [OI*]-63 μm fine-structure emission, these transitions are natural candidates for tracing the total HI content, as they are likely to primarily originate from the same gas. Additionally, OI is closely linked to HI by a charge-exchange reaction. The important role [CII*]-158μm emission plays for cooling makes it a viable candidate for estimating the cool-

15

ing rate in the ISM. The goal of this thesis is to detect absorption lines of CII and OI from GRB afterglow spectra and use the column densities to characterize the ISM of a sample of galaxies at high redshifts.

2 Observations

The data used in this thesis is a sample of ten GRBs observed with the VLT/UVES spectrograph from Ledoux et al. (2009).

2.1 The UVES Spectrograph

UVES (Ultraviolet and Visual Echelle Spectrograph) is a high-resolution cross-dispersed echelle spectrograph of the VLT (Very Large Telescope) located at the Nasmyth B focus of UT2. It can operate with high efficiency at wavelengths ranging from the atmospheric cut-off at 300 nm to the long wavelength limit of CCDs at $\sim$1100 nm. The spectral resolution R= $\lambda/\Delta\lambda$ determines the ability to distinguish spectral lines with small separations, and the high resolution of UVES enables the study of the narrow absorption lines of cold gas. Table 1 shows the accessible wavelength range, maximum resolving power, and an estimate of the limiting magnitude of the blue and red arm that the light beam from the telescope is split into.

	Blue	Red
Wavelength range (nm)	300 - 500	420 - 1100
Maximum resolution ($\lambda/\Delta\lambda$)	80000	11000
Magnitude limits	17 - 18	18 -19

Table 1: The accessible wavelength range, maximum resolving power and limiting magnitude estimate of the UVES spectrograph.

2.2 Spectroscopic Data

The data used in this project is a sample of ten GRBs detected by the UVES spectrograph, with redshifts spanning $1.96887 \leq z \leq 3.9857$, and wavelengths spanning $3044\text{Å} \leq \lambda \leq 10429\text{Å}$. The GRBs are listed in Table 2 along with the corresponding redshifts of the systems.

GRB	z
021004	2.32914
050730	3.9857
050820A	2.61467
050922C	2.619985
060607A	3.07476
071031	2.69248
080310	2.42743
080413A	2.43489
081008	1.96887
130610	2.092

Table 2: GRB sample detected by UVES and the corresponding redshifts of the systems.

As motivated in Section 1.4, the absorption lines of interest for this project are [CII*]λ1335, [OI*]λ1304 and [OI**]λ1306. The column densities are inferred by fitting Voigt profiles to the absorption lines.

2.3   Voigt Profile Fitting

The Voigt profile frequently emerges in spectroscopy and is commonly used for spectral line fitting in absorption systems like GRBs. Mathematically, it is a convolution of a Lorentz distribution and a Gaussian distribution. Near the line center, the Voigt function resembles a Gaussian, while the wings look like those of a Lorentzian.

2.3.1   The Voigt-Hjerting Function and Tepper-García Approximation

One can describe the absorption line arising from a given transition by its optical depth τ. Using the column density N of a given element X, a set of atomic parameters describing the line strength f_i, the damping constant Γ_i, and the resonance wavelength λ_i, one can express the optical depth of transition i as

$$\tau_{i,X}(\lambda) = K_i N_X a_i H[a_i, x(\lambda)], \tag{3}$$

where $H[a_i, x(\lambda)]$ is the Voigt-Hjerting function, and K_i and a_i are defined as

$$K_i \equiv \frac{e^2 \sqrt{\pi} f_i \lambda_i}{m_e c b} \text{ and } a_i \equiv \frac{\lambda_i \Gamma_i}{4\pi b}, \tag{4}$$

with e being the elementary charge, m_e the mass of the electron, c the speed of light and b the broadening parameter. The Voigt-Hjerting function

$$H[a_i, x(\lambda)] \equiv \frac{a_i}{\pi} \int_{-\infty}^{\infty} \frac{e^{-y^2}}{[x(\lambda) - y]^2 + a_i^2} dy \tag{5}$$

describes the single absorption-line profile. Here, $y = v/b$ is the velocity of the absorbing atom in terms of the broadening parameter b, and $x(\lambda) = (\lambda - \lambda_i)/\lambda_D$ is the re-scaled wavelength, where $\lambda_D = b\lambda_i/c$ is the Doppler wavelength.

The numerical integration of the Voigt-Hjerting function can be rather cumbersome, and hence an approximation derived by García (2006), containing only one fourth-order polynomial and Gaussian functions, may be used to model Voigt profiles with an accuracy of 10^{-4} or better in a more simple manner:

$$H(a_i, x) \approx H_0 - \frac{a_i}{x^2(\lambda)\sqrt{\pi}}[H_0^2(4x^4 + 7x^2 + 4 + 1.5x^{-2}) - 1.5x^{-2} - 1], \tag{6}$$

where $H_0 = e^{-x^2}$. The resulting transmittance is

$$I(\lambda) = \exp \tau(\lambda). \tag{7}$$

This approximation is used in the Python package VoigtFit by Krogager (2018), which was used for the absorption line fitting.

2.3.2   VoigtFit

VoigtFit enables the fitting of transitions of different ions simultaneously through an interactive window. As input, the spectral data is loaded as a table containing flux, wavelength, and errors. The transitions to be fit must then be specified, in this case, [CII*]λ1335, [OI*]λ1304 and [OI**]λ1306. In the interactive interface, the observed peaks can be selected, and the continuum defined. VoigtFit returns the redshifts and calculates the column density by equating the initial broadening parameter to the resolution element.

2.3.3   Absorption Line Detection

We detected CII*, OI*, and OI** in six of the ten GRBs from the sample. Out of these, CII* absorption lines were detected at the redshift of the GRB system in five out of six cases, OI* lines in four of them, and OI** lines in three.

3 Analysis

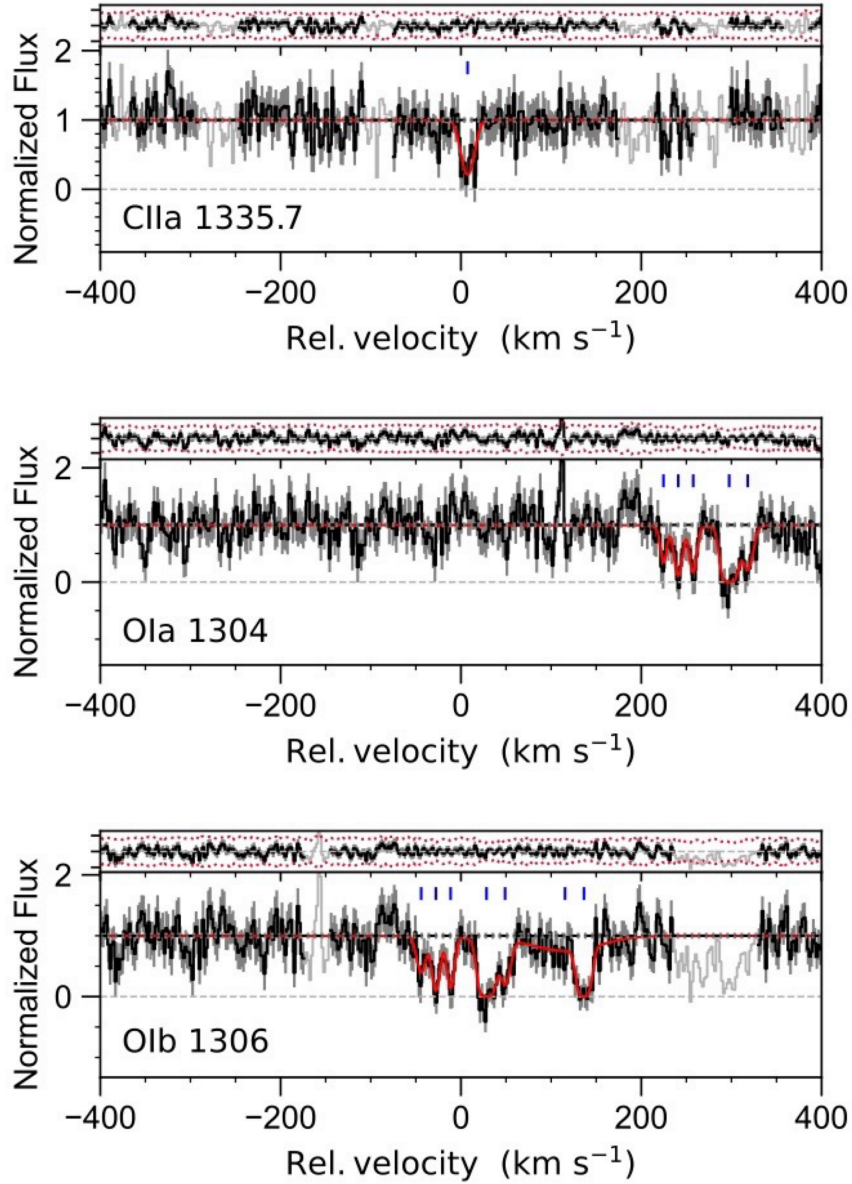## 3.1 Absorption Line Detection

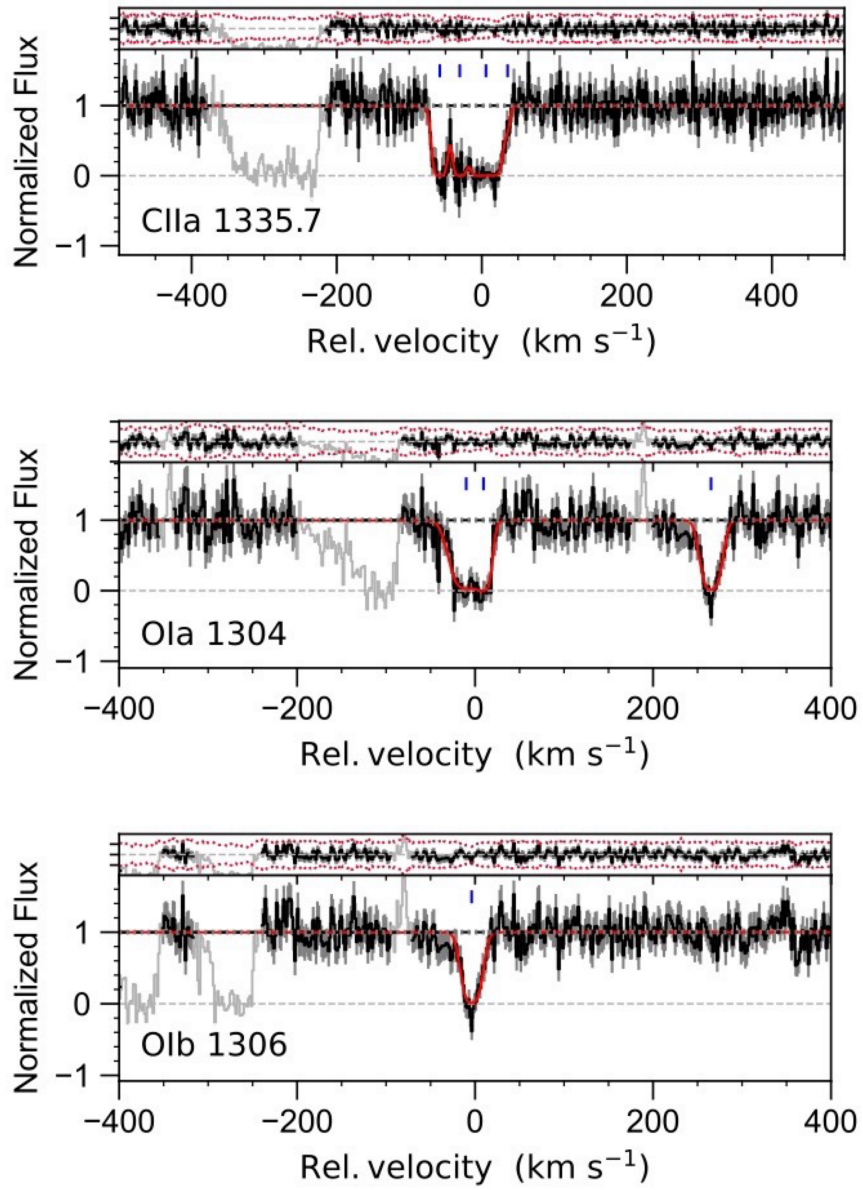Figure 3: Voigt profile fit of the absorption spectrum from GRB021004.

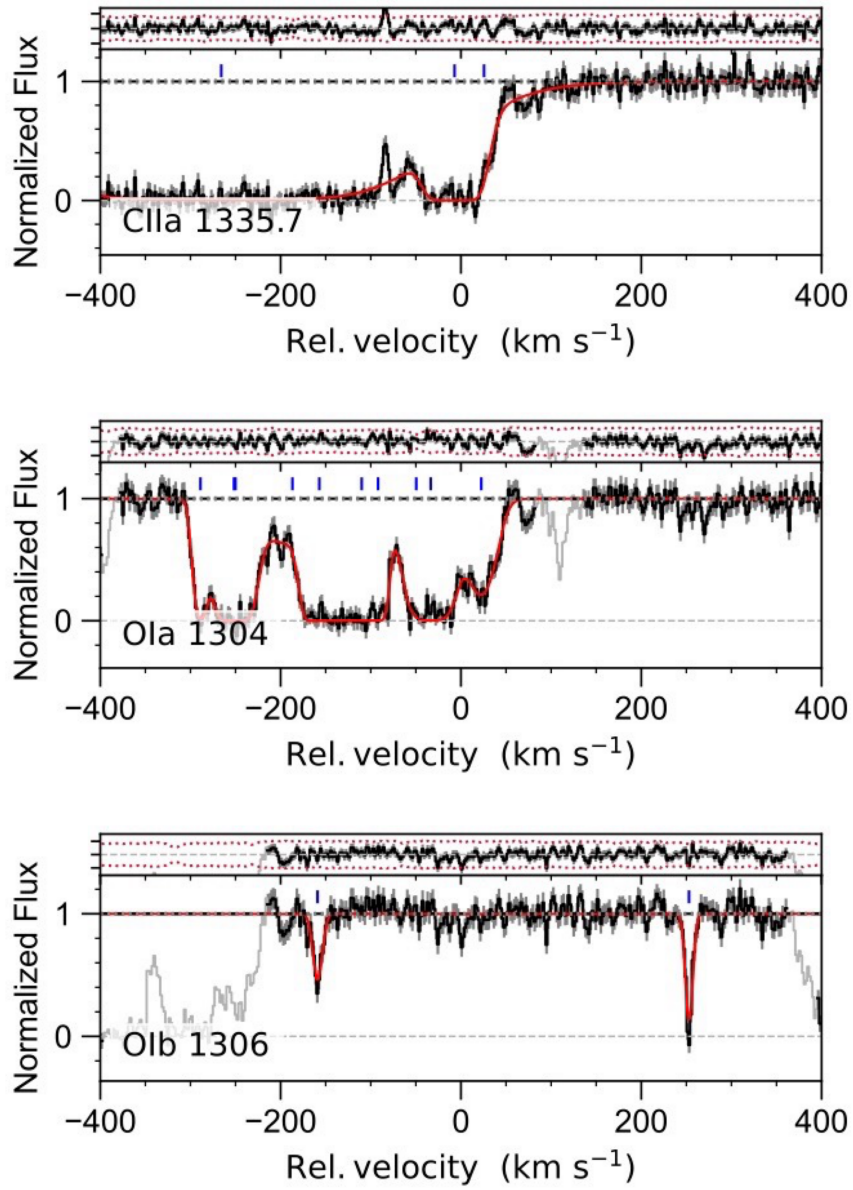Figure 4: Voigt profile fit of the absorption spectrum from GRB050730.

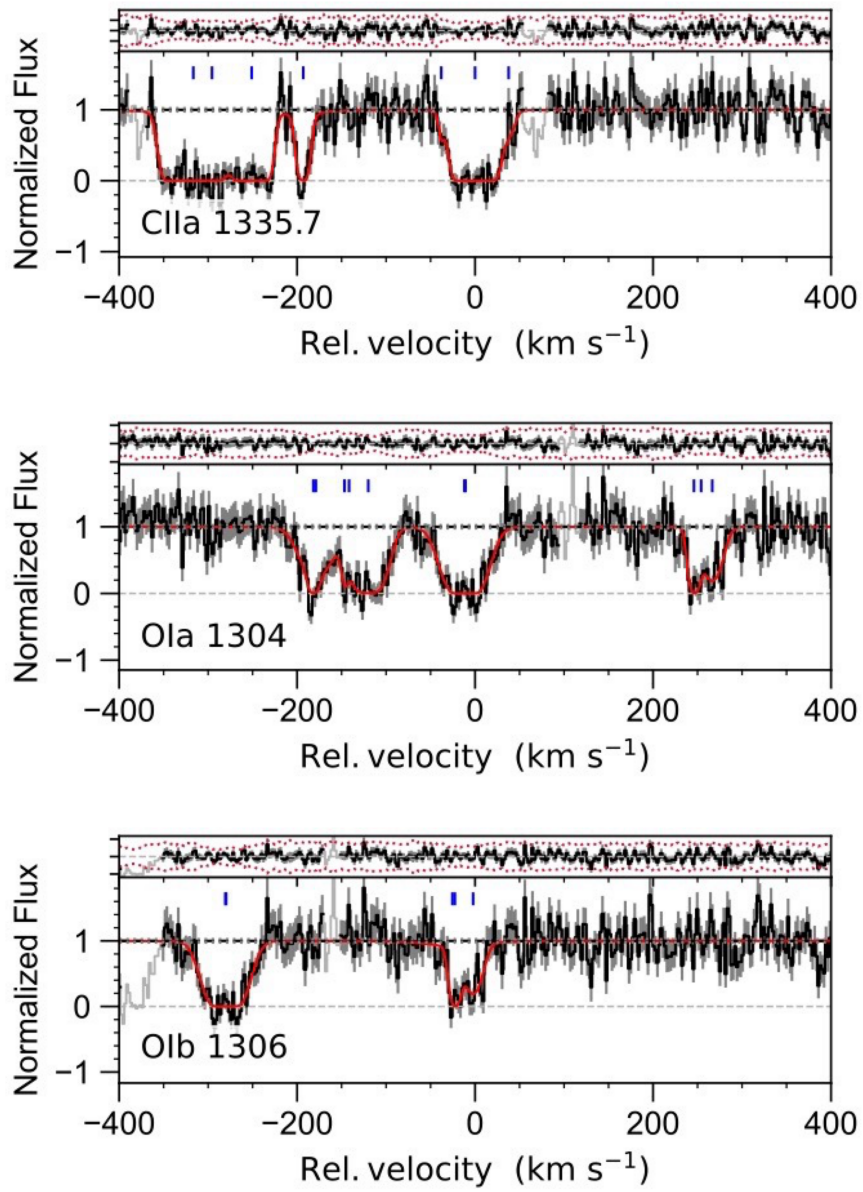Figure 5: Voigt profile fit of the absorption spectrum from GRB050820A.

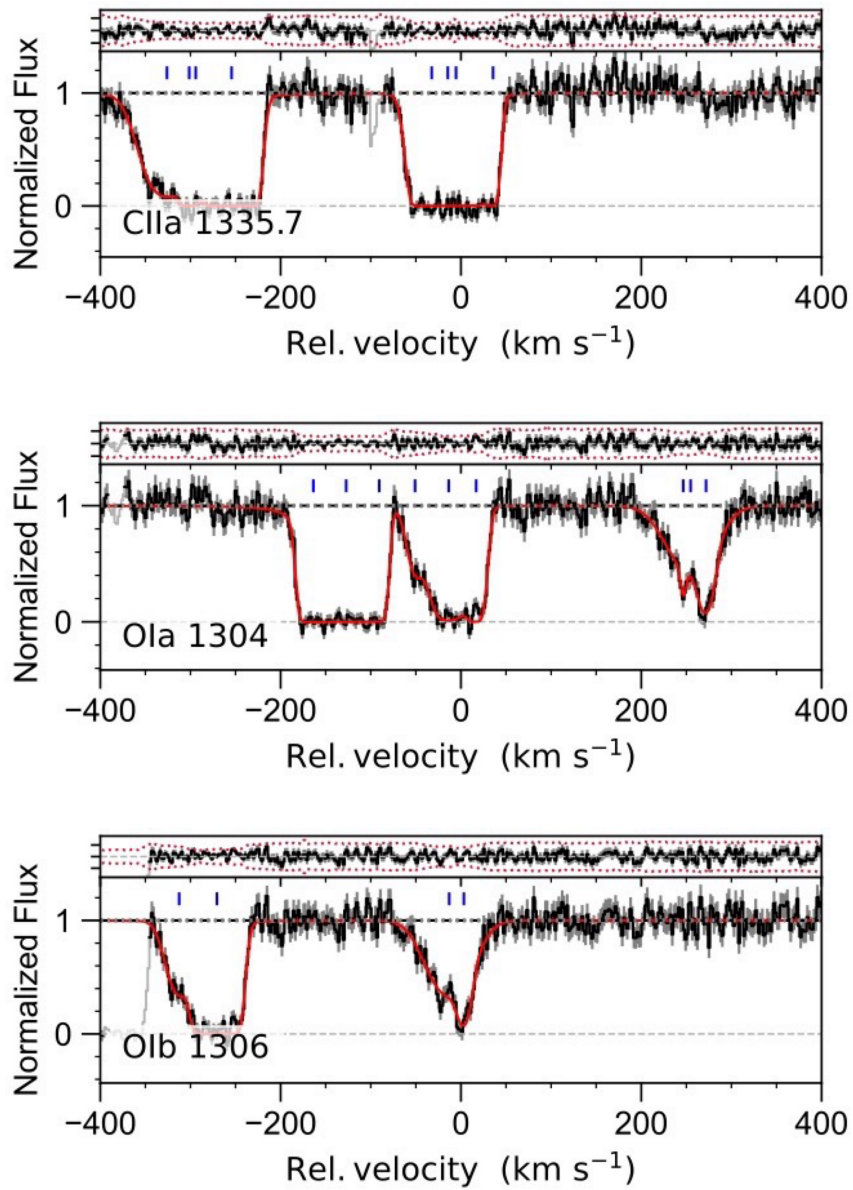Figure 6: Voigt profile fit of the absorption spectrum from GRB050922C.

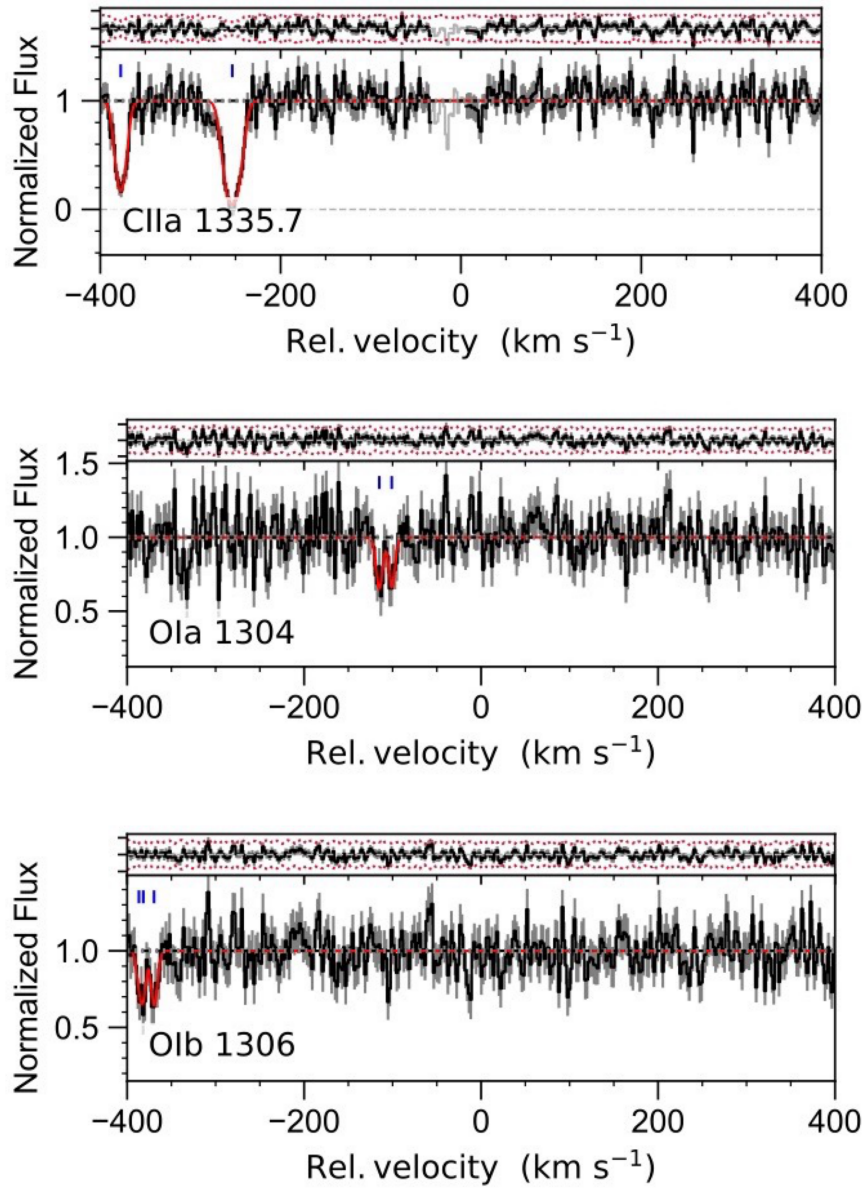Figure 7: Voigt profile fit of the absorption spectrum from GRB071031.

Figure 8: Voigt profile fit of the absorption spectrum from GRB080310.

Figures 3 to 8 show the absorption spectra, along with the fitted Voigt profile, shown as the red curve, of the GRBs for which the desired lines ([CII**]1335.7, [OI*]1304.858 and [OI**]1306.029) could be detected.

GRB060607A has been excluded as none of the desired absorption lines could be identified. GRB080413A, GRB081008, and GRB130610 are also not included, as the lines were not covered by the spectrum.

For GRB021004, shown in Figure 3, the [CII*]1335.7 line is detected at redshift z ≈ 2.329, which corresponds to the redshift of the system. Several absorption components were detected for [OI*]1304.858 and [OI**]1306.029, but not at zero relative velocity. Figure 4 clearly shows troughs for all three lines in the spectrum of GRB050730 at the redshift of the system. In the top panel of Figure 5, a strong break in the spectrum can be seen. The column densities obtained for this GRB are considered to be unreliable. The spectrum of GRB050922C shows absorption features for all three lines around the redshift of the system and is shown in Figure 6. Figure 7 shows that absorption components for all of the lines are also detected in the spectrum of GRB071031. The lines are also detected in the spectrum of GRB080310, shown in Figure 8, but not at the velocity of the GRB.

GRB	z	logN(HI)	logN(CII*)	logN(OI*)	logN(OI**)
021004	2.32914	19.6 ± 0.3	14.746 ± 0.083	14.085 ± 0.163	14.558 ± 0.122
050730	3.9857	22.15 ± 0.05	13.866 ± 0.783	15.079 ± 0.149	14.717 ± 0.148
050820A	2.61467	21.00 ± 0.10	16.718 ± 0.059	14.946 ± 0.394	13.770 ± 0.071
050922C	2.619985	21.55 ± 0.10	14.192 ± 0.631	15.425 ± 0.178	15.172 ± 0.419
071031	2.69248	22.15 ± 0.05	15.461 ± 0.177	15.413 ± 0.121	14.870 ± 0.044
080310	2.42743	18.70 ± 0.10	15.269 ± 0.041	13.724 ± 0.178	13.421 ± 0.257

Table 3: CII*, OI* and OI** column densities shown alongside the HI column density (Cucchiara et al., 2015) and the redshift of system.

3.2 Conversion Factors

From the approach presented by Heintz et al. (2021), the HI gas mass of the host galaxies can be inferred using direct measurement of the [CII]-to-HI conversion factor. This approach was adopted here to also obtain the [OI]-to-HI conversion factors.

3.2.1 [CII]-to-HI Conversion Factor

Singly ionized carbon, $CII(1s^2 2s^2)2p^2 P^0$, splits into two fine-structure levels, with $^2P^{1/2}$ being the ground state and $^2P^{3/2}$ the excited state, denoted CII*. These states have an energy separation of 63.42 cm^{-1}, and the transition $^2P^{3/2} \rightarrow {}^2P^{1/2}$ produces the [CII*]-158 μm line, giving rise to the [CII*]$\lambda 1335.7$ line. Using the transition energy, ν_{ul}, and the Einstein coefficient for spontaneous decay to the ground $^2P^{1/2}$ state, A_{ul}, Heintz et al. (2021) presents the "column" luminosity of the line as

$$L^c_{[CII]} = h\nu_{ul}A_{ul}N_{[CII^*]},\qquad(8)$$

where h is Planck's constant, $\nu_{ul} = 1900.537$ GHz and $A_{ul} = 2.4 \times 10^{-6}s^{-1}$. The line-of-sight HI column mass density is determined from

$$M^c_{HI} = m_{HI}N_{HI}.\qquad(9)$$

This is then used to compute the line-of-sight [CII]-to-HI conversion factor:

$$\beta_{[CII]} \equiv \frac{M_{HI}}{L_{[CII]}} = \frac{M^c_{HI}}{L^c_{[CII]}} = \frac{m_{HI}N_{HI}}{h\nu_{ul}A_{ul}N_{[CII^*]}}.\qquad(10)$$

3.2.2 [OI]-to-HI Conversion Factors

The ground state of neutral oxygen splits into three fine-structure levels in the n = 2 shell. The transition $^3P_2 \rightarrow {}^3P_1$ connects the lower and middle

fine-structure levels and produces the [OI*]-63.18 μm line. The $^3P_1$ level is further connected to the exited electronic state $^3S_1$ in the n = 3 shell, giving rise to the [OI*]1304.858 line. The middle and upper fine-structure levels are connected by the [OI**]-145.53 μm line, arising from the transition $^3P_1 \to {}^3P_0$. The $^3P_0$ level is also connected to the exited electronic state $^3S_1$ in the n = 3 shell and gives rise to the [OI**]1306.029 line.
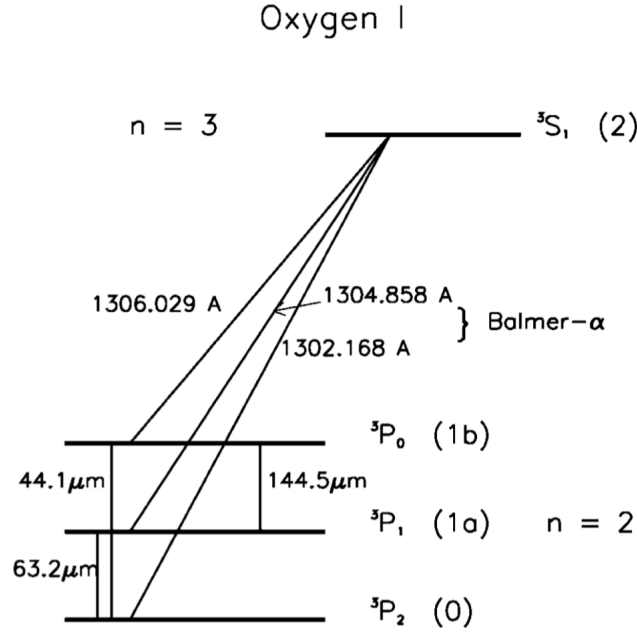

Figure 9: Schematic representation of the OI fine structure transitions giving rise to the spectral lines of interest. Reprinted from Hernández-Monteagudo et al. (2007).

The transition energy for [OI*]-63.18 μm is $\nu = 4744.777$ GHz and the Einstein coefficient for spontaneous decay to the $^3P_2$ state is $A_{ul} = 8.91 \times 10^{-5}$ s^{-1}. Adopting the same approach as for the [CII]-to-HI conversion factor to determine the [OI*]-to-HI conversion factor yields

$$\beta_{[OI^*]} \equiv \frac{M_{HI}}{L_{[OI^*]}} = \frac{M_{HI}^c}{L_{[OI^*]}^c} = \frac{m_{HI}N_{HI}}{h\nu_{ul}A_{ul}N_{[OI^*]}}. \tag{11}$$

Similarly, for OI**, the conversion factor is defined as

$$\beta_{[OI^{**}]} \equiv \frac{M_{HI}}{L_{[OI^{**}]}} = \frac{M_{HI}^c}{L_{[OI^{**}]}^c} = \frac{m_{HI}N_{HI}}{h\nu_{ul}A_{ul}N_{[OI^{**}]}}, \qquad (12)$$

where, for [OI**]-145.53 μm, $\nu = 2060.069$ GHz and $A_{ul} = 1.75 \times 10^{-5}$ s^{-1}.

GRB	[X/H]	β_{CII}	β_{OI^*}	$\beta_{OI^{**}}$
050730	-2.18 ± 0.11	4.4 ± 0.8	1.17 ± 0.16	2.61 ± 0.16
050820A	-0.39 ± 0.1	0.35 ± 0.12	0.2 ± 0.4	2.40 ± 0.12
050922C	-1.82 ± 0.11	3.4 ± 0.6	0.23 ± 0.20	1.6 ± 0.4
071031	-1.73 ± 0.05	2.76 ± 0.18	0.84 ± 0.13	2.45 ± 0.07
080310	≤ -1.91 ± 0.13	-0.50 ± 0.11	-0.92 ± 0.20	0.45 ± 0.28

Table 4: [CII]-to-HI (β_{CII}), [OI*]-to-HI (β_{OI^*}), and [OI**]-to-HI ($\beta_{OI^{**}}$) conversion factors.

3.3 The Phases of the Neutral Interstellar Medium

As mentioned in Section 1.2.1, the neutral interstellar medium (ISM) is modeled as consisting of two stable phases: the cold neutral medium (CNM), with typical temperature T $\lesssim$ 100 K, and the warm neutral medium (WNM), with typical temperature T $\lesssim$ 10^4 K (Field et al., 1969). In this model, where the two phases coexist in pressure equilibrium (Wolfire et al., 1995), the thermal balance is a result of the cooling, predominantly from line emission, and the heating, mainly through the photoelectric effect and cosmic rays. A significant contributor to the cooling of the CNM is the [CII*]-158μm transition. Adopting the method for estimating the cooling rate from Wolfe et al. (2005), as well as the method for showcasing the bimodality of the CII*/CII ratio from Balashev et al. (2021), we may estimate whether the GRBs considered in this thesis probe warm or cold neutral medium.

3.3.1 Cooling Rate

When arguing for the bimodality of [CII*]-158 μm cooling rate l_c, Wolfe et al. (2008) defines l_c using the column density, N(CII*), of the excited ^{2}P$_{3/2}$ state of C$^+$ as

$$l_c \equiv \frac{N(CII^*)}{N_{HI}} A_{ul} h \nu_{ul}, \tag{13}$$

where N_{HI} is the HI column density, $A_{ul} = 2.4 \times 10^{-6}$ s^{-1} is the Einstein coefficient for spontaneous photon decay to the ground $^2P_{1/2}$ state and $\nu_{ul} = 1900.537$ GHz is the energy for this transition.

Wolfe et al. (2008) found that the distribution of the [CII*]-158 μm cooling rate showed peaks at $l_c = 10^{-27.4}$ and $l_c = 10^{-26.6}$ erg s^{-1} H^{-1} with a separation at $l_c^{crit} \approx 10^{-27}$.

3.3.2 CII*/CII Ratio

Balashev et al. (2021) shows that the bimodality in the CII cooling rate that was found by Wolfe et al. (2008) reflects a bimodality in the CII*/CII-metallicity plane as a natural result of phase segregation in the neutral interstellar medium. As opposed to the column density of CII*, the CII column density cannot be obtained directly from the absorption spectra because the line is heavily saturated. Therefore, to estimate the CII*/CII ratio, Balashev et al. (2021) uses the metallicity as a proxy for the carbon abundance and defines this ratio, R_C, as

$$R_C = \frac{N(CII^*)}{N(HI)(C/H)_\odot \langle Z \rangle} \equiv \langle R_C \rangle, \tag{14}$$

where $(C/H)_\odot = 8.47 \pm 0.05$ (Asplund et al., 2009) is the solar abundance and $\langle Z \rangle$ is the overall metallicity.

To determine whether the GRBs are probing WNM or CNM, the CII*/CII ratios are separated into the GRBs with $l_c < 10^{-27}$ and $l_c > 10^{-27}$ probing WNM and CNM, respectively.

GRB	l_c	R_C
050730	-27.8 ± 0.785	-7.252 ± 0.792
050820A	-23.9 ± 0.116	-4.55 ± 0.792
050922C	-26.874 ± 0.639	-6.406 ± 0.654
071031	-26.205 ± 0.184	-5.767 ± 0.22
080310	-22.947 ± 0.108	-2.449 ± 0.169

Table 5: Cooling rates l_c and CII*/CII ratios R_C.

4 Results

4.1 Metallicity

First, we compare the GRB sample evaluated here against a larger, more statistical sample of GRBs from VLT/X-shooter, VLT/FORS1, VLT/FORS2, NOT/A1FOSC, Keck/ESI, Keck/LRIS, Keck/HIRES, and Gemini/GMOS taken from Cucchiara et al. (2015). This comparison helps us examine whether we are only probing a particular part of the parameter space or if our sample covers the overall underlying distribution.
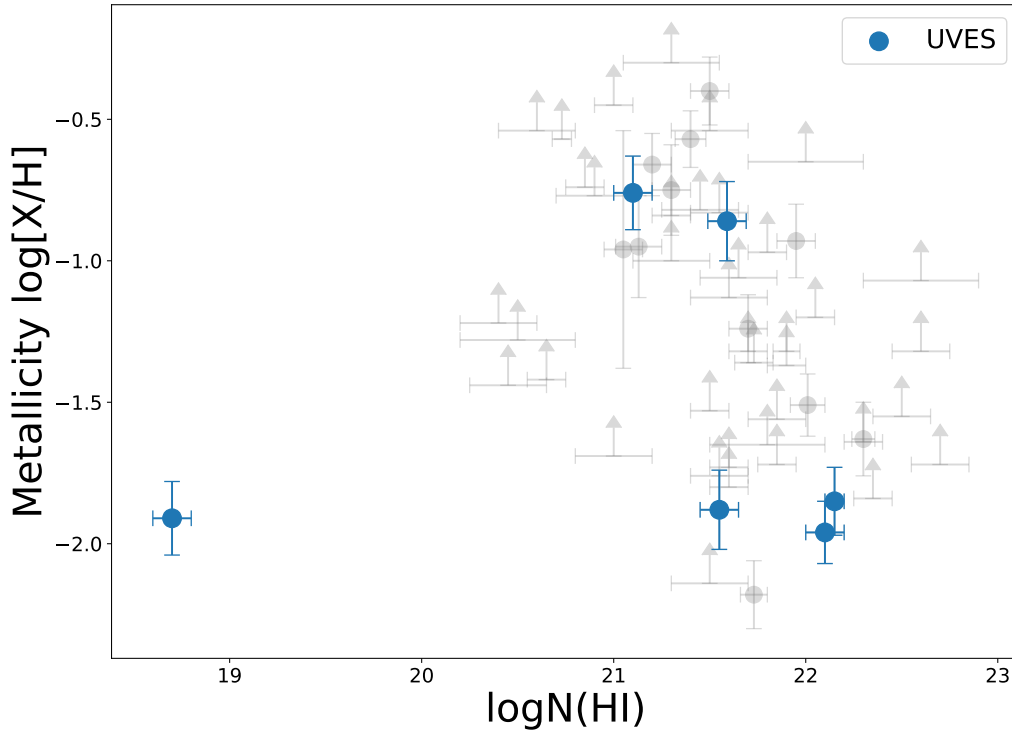
Figure 10: Metallicities, taken from Cucchiara et al. (2015) and Ledoux et al. (2009), plotted against HI column density. The blue dots represent the GRBs evaluated in this thesis and the grey markers represent GRBs from the larger GRB sample.

Figure 10 shows the GRBs evaluated in this thesis as blue dots, and the larger sample of GRBs is shown in grey. We find that four of the GRBs (050730, 050922C, 071031, and 080310) from our sample lie in the lower metallicity region in comparison with the larger GRB sample. GRB050820A and 080413A appear to have metallicities of similar values as most of the GRBs with similar HI column densities from the larger sample. GRB080310 stands out by having significantly lower HI column density than the rest, which is to be expected as the larger sample only consists of DLAs.

4.2 Conversion Factors

Next, we plotted the derived conversion factors against the metallicity to see if they follow the expected anti-correlation that has been found in nearby galaxies (Hughes et al., 2013; Bothwell et al., 2013; Lara-López et al., 2013; Brown et al., 2017; Stark et al., 2021). We naturally expect this anti-correlation since the metallicity is given as $\log{[X/H]}$, where X is a heavy element, and our conversion factors are given as M_{HI}/L_X.
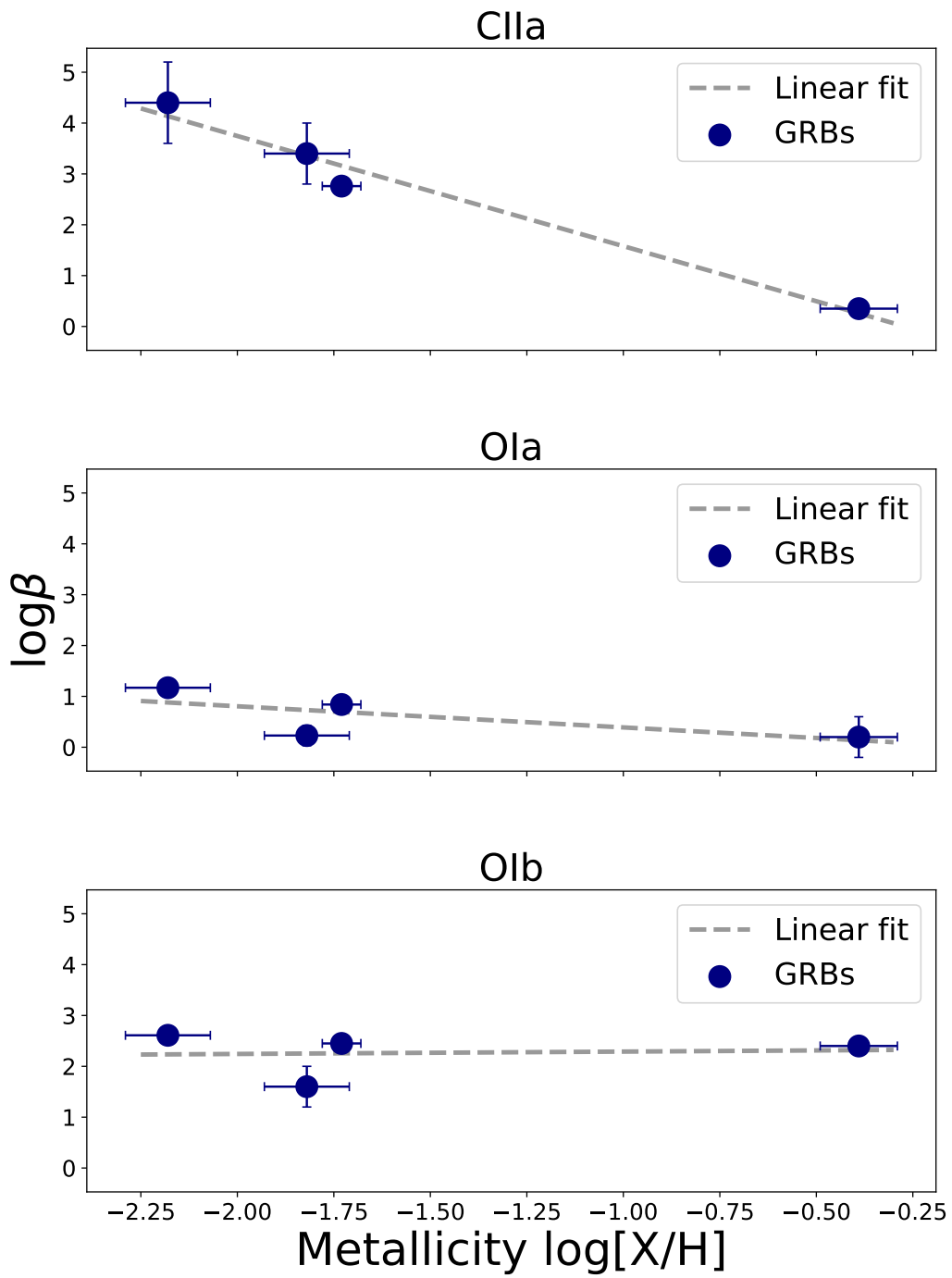
Figure 11: Metallicity evolution of the conversion factors.

From the top panel in Figure 11, we find that the [CII]-to-HI conversion factor appears to follow the trend of linear decrease with increasing metallicity, which was also seen in Heintz et al. (2021). This trend is weaker for the [OI*]-to-HI conversion factor and not apparent at all for the [OI**]-to-HI conversion factor, which seems to be independent of metallicity.

4.3 CII*/CII ratio

To examine whether the GRBs from our sample probe WNM or CNM, we plot the R_C ratio against the metallicity to see if the bimodality in the cooling rate is reflected in the CII*/CII metallicity plane.
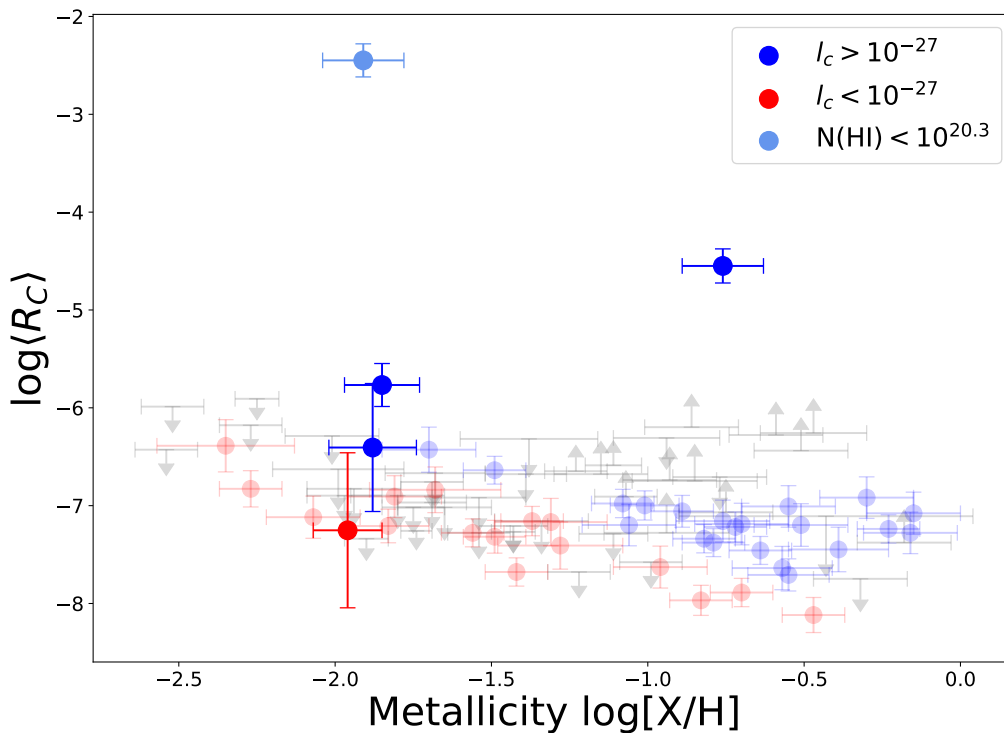

Figure 12: Metallicity evolution of the CII*/CII ratio, R_C. The blue and red dots represent the GRBs for which the cooling rates correspond to $l_c > 10^{-27}$ and $l_c < 10^{-27}$ respectively. The smaller dots represent a larger DLA sample, taken from Wolfe et al. (2008), shown for comparison.

From Figure 12, we find that R_C seems to follow the trend of decreasing with increasing metallicity for both CNM and WNM, being around one order of magnitude higher in the CNM than in the WNM, as was also found by Balashev et al. (2021). The obvious exception to this is the two outliers with significantly higher R_C values than the rest of the sample from both this work and the larger GRB sample. GRB080310 has the highest R_C value and deviates significantly from the rest of the sample. This was, however, expected given that the HI column density obtained from this GRB was significantly lower than for the rest of the sample. GRB050820A has a CII*/CII ratio of $R_C \approx 4.55$, which clearly distinguishes it from other GRBs of similar metallicity. As mentioned in Section 3.1, [CII*]1335.7 in the spectrum of GRB050820A did not provide a reliable column density, which was found to be considerably larger than for the rest of the sample and can be seen in Table 3. Only one of the GRBs evaluated, GRB050730, has a cooling rate $l_c < 10^{-27}$ and is thus predicted to probe WNM. The rest seem to probe CNM.
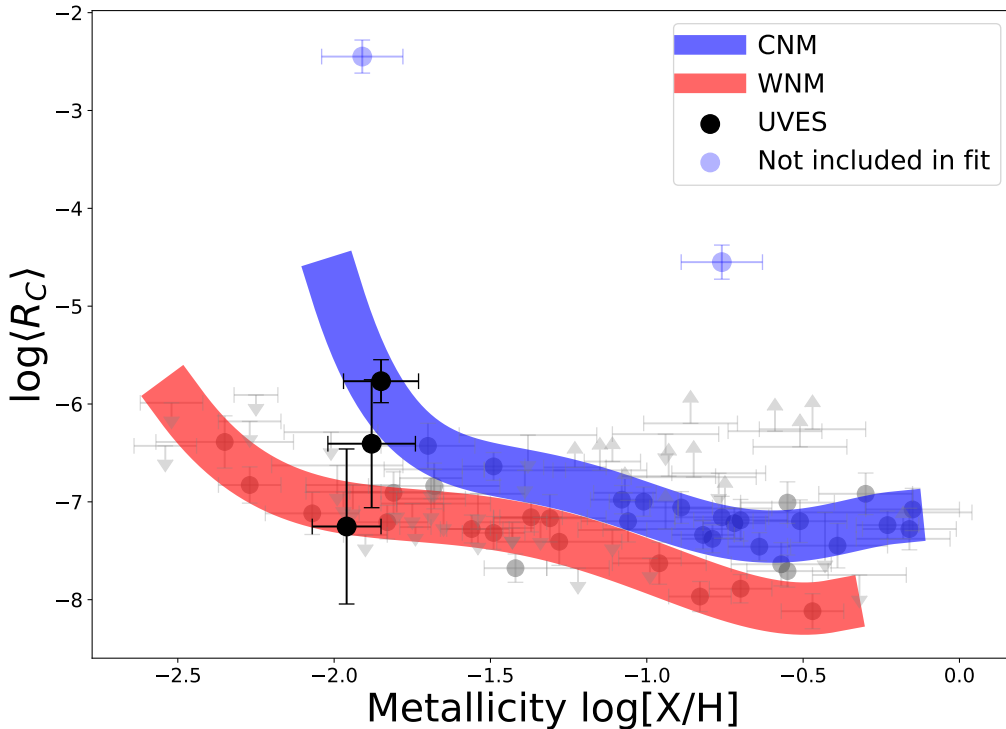

Figure 13: Blue and red curves showing the domains of R_C for GRBs probing CNM and WNM respectively.

In Figure 13, we plot the curves for CNM in blue and WNM in red to show
their domains. The two outliers have not been included in the fit. The grey
markers represent the DLA sample from Wolfe et al. (2008), which was used
in the fit.

5 Discussion

The conversion factors provide an estimate for the average abundance ratios along the line-of-sight through the ISM of high-redshift star-forming galaxies without using scaling relations or assuming anything about the physical state of the gas. It is not necessary for the CII or OI emitting gas to be directly associated with the HI gas, nor is it required that the gas originates from the HI reservoirs for the conversion factors to be applicable.

5.1 Metallicity Dependence

The observed anti-correlation between the [CII]-to-HI conversion factor and metallicity, seen in the top panel of Figure 11, is in good agreement with our expectations based on the multiple studies that have found such an anti-correlation in nearby galaxies (Hughes et al., 2013; Bothwell et al., 2013; Lara-López et al., 2013; Brown et al., 2017; Stark et al., 2021).

As mentioned in Section 1.3.1, GRBs are related to the death of massive stars and are thus predicted to probe the regions where star formation occurs. HI and H_2 are the fuel of star formation, and it is therefore expected that there are relations between HI mass, stellar mass, and star-formation rate (SFR) in a galaxy. Consequently, we should also expect an anti-correlation between the HI fraction and metallicity.

The Kennicutt-Schmidt law predicts the relationship between HI mass and SFR through the correlation that is found between gas surface density and SFR, but this also includes H_2 and the scatter is considerable (~ 0.2 dex) (Kennicutt, 1998). The HI mass is therefore considered to only be one of the various factors regulating the SFR and is only indirectly related to it as star formation happens in molecular clouds. Therefore, it is easier to establish a relationship between H_2 and SFR, but the insufficient amount of large-scale CO surveys makes an empirical study of this relationship challenging. As described in Section 1.1, HI gas must accrete into the galaxy to cool and form H_2, and inferring the HI gas mass can therefore reveal information about the H_2 content (Leroy et al., 2008; Wong et al., 2016). Several studies have supported the correlation between HI mass and SFR (Mirabel & Sanders, 1988; Doyle & Drinkwater, 2006).

Therefore, we expect a correlation between HI and SFR, but we should also expect an anti-correlation between HI and metallicity. This is because of the prediction that metal-poor gas fuels the star-formation process, and we would therefore expect higher SFR, and hence a higher fraction of HI, with lower metallicities. An increase in the accretion of HI leads to higher gas mass and hence dilution of the heavy elements, which enhances star formation. This is supported by the fundamental metallicity relation (FMR), which also suggests that low metallicity is linked to higher SFR for a given stellar mass (Curti et al., 2019). Alternatively, the anti-correlation can be explained by intense outflows of heavy elements from the star-forming regions by stellar winds and supernovae.

5.1.1 [OI]-to-HI

The anti-correlation with metallicity appears to be weaker when looking at the [OI*]-to-HI conversion factors, shown in the middle panel of Figure 11. We note that the HI fraction relative to the oxygen lines is smaller compared to HI relative to CII. This is not surprising as oxygen is the most abundant metal in the ISM. For [OI**]-to-HI, such an anti-correlation is not observed at all. In fact, the conversion factor seems to be approximately constant across our sample. However, it must be noted that the sample has relatively low metallicities and that only one of the GRBs is at redshift $z \approx 4$, while the rest is at z $\approx$ 2.4 - 2.6. The results are still interesting, as they show a possibility of inferring the HI gas mass from the conversion factors when the metallicity is unknown. OI is a very attractive candidate for tracing HI, as they are closely linked by a charge-exchange reaction:

$$O^+ + H \longleftrightarrow O + H^+, \tag{15}$$

implying that [OI/HI] $\approx$ [O/H] (Field & Steigman, 1971).

5.2 Evolution with Redshift

The validity of the conversion factors can be supported by looking at how they evolve with redshift. Given that we expect a decrease in metallicity at higher redshifts, the expected anti-correlation between the HI fraction and

metallicity indicates that we should also expect an increase in HI at higher redshifts. Looking at the redshift evolution of the conversion factors, shown in Figure 14, we find a steady increase in the values of the conversion factors with higher redshifts, including [OI**]-to-HI, for which the anti-correlation with metallicity was not found. The [OI]-to-HI conversion factors evolve as expected with redshift, which suggests, given that metallicity depends on redshift, that the OI-to-HI conversion factors are less dependent on metallicity. This implies that if such a constant abundance ratio with varying metallicity, as was found for [OI**]-to-HI, is valid, one could infer the HI gas mass from this conversion factor at a given redshift without knowing the metallicity.
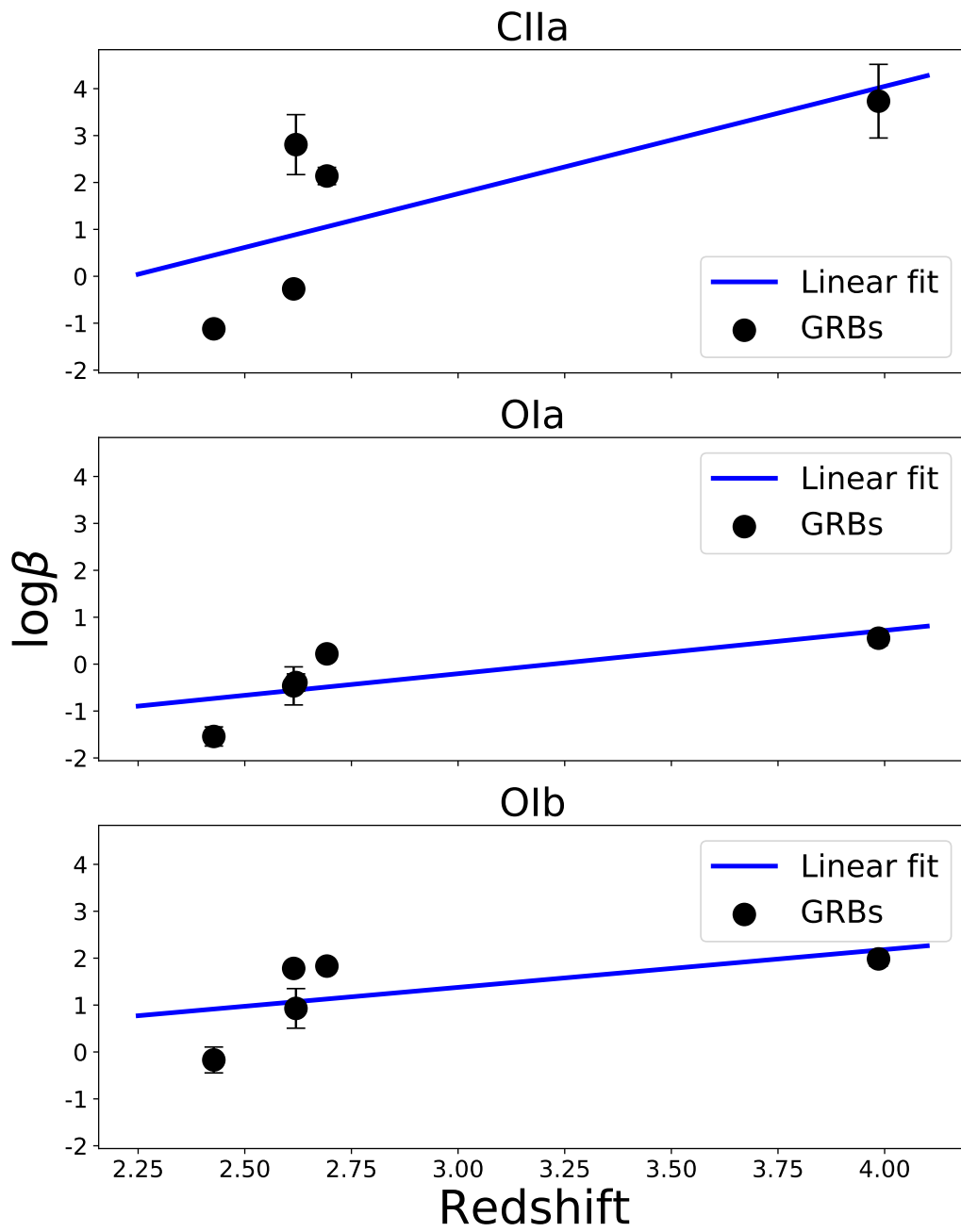
Figure 14: Redshift evolution of the conversion factors.

5.3 Relation to Cooling Rate and CII*/CII

Since the WNM is only comprised of HI and no molecular gas, we would expect the GRBs probing WNM to have higher HI fractions. Consequently, in the colder gas, we expect more molecules to form, and hence less HI and higher cooling rates. As shown in Figure 12, the bimodality in the [CII*]-158 μm cooling rate l_c reflects a bimodality in the CII^*/CII metallicity plane. The CII^*/CII ratio, R_C, is given in equation 14 from where we can see that an anti-correlation between HI and R_C should be expected. All of our conversion factors show a linear decrease with increasing R_C, which can be seen in Figure 15.
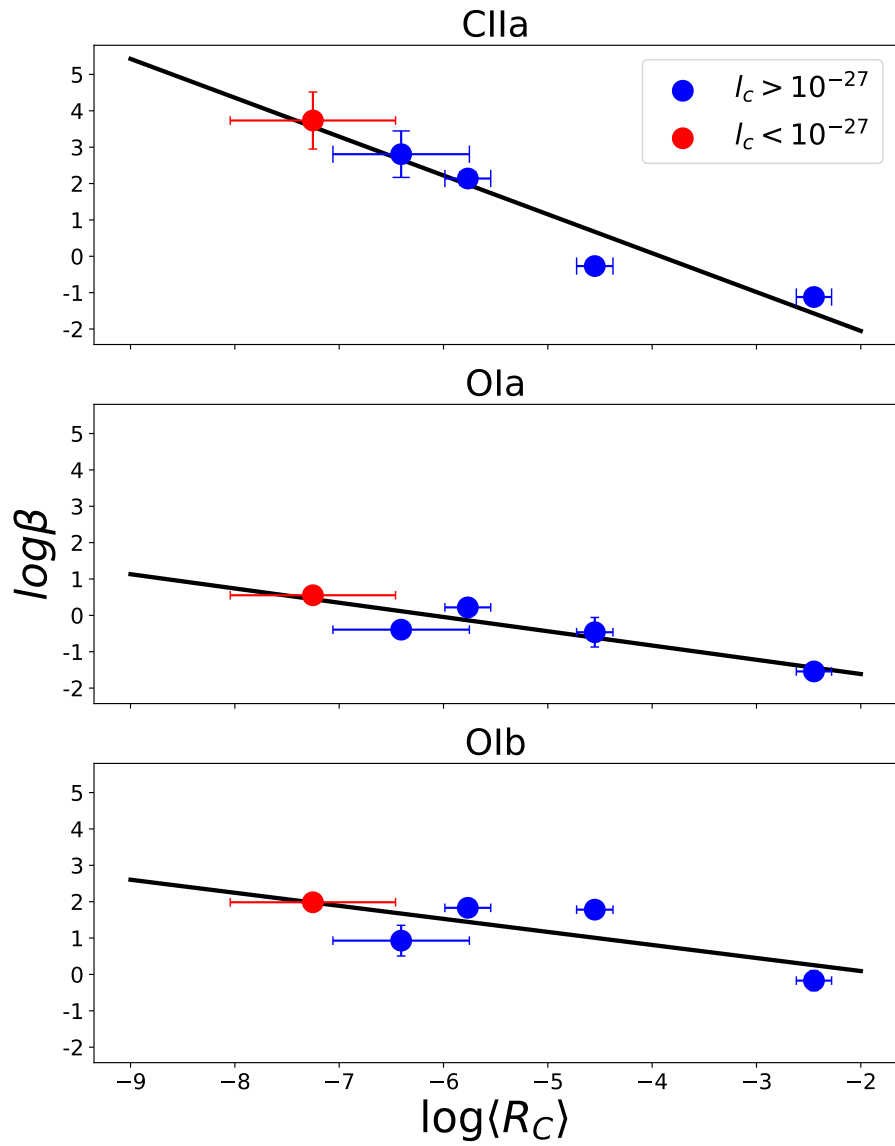
Figure 15: Evolution of the conversion factors in the CII*/CII metallicity plane.

6   Summary and Conclusion

In this thesis, I have analyzed a sample of GRB afterglows observed at redshifts z $\sim$ 2-4 with the VLT/UVES spectrograph to investigate the interstellar environment of the host galaxies. I have calculated the [CII]-to-HI, [OI*]-to-HI, and [OI**]-to-HI conversion factors from the column densities inferred from fitting Voigt profiles to the absorption spectra. Furthermore, I have estimated the cooling rates to determine whether the GRBs probe warm or cold neutral medium.

From my sample, I detected absorption lines from CII*, OI* and OI** in six of the ten GRB spectra. Out of this sample, I was able to calculate conversion factors in four cases using available metallicity measurements. I found a strong anti-correlation between [CII]-to-HI and metallicity, and a weaker anti-correlation for [OI*]-to-HI. The [OI**]-to-HI conversion factor appeared to be independent of metallicity. All three conversion factors showed a steady increase with redshift, and I found an anti-correlation between all of the conversion factors and the CII*/CII ratio. It should be noted that our sample is very limited and, therefore, does not allow for robust constraints, but the relatively constant conversion factor with respect to metallicity that was found for [OI**]-to-HI is an interesting result that merits further investigation. The conversion factors may enable the inference of the HI gas mass of star-forming galaxies at high redshifts, for which current radio telescopes cannot detect the hyperfine 21-cm HI transition.

References

Abel, T., Anninos, P., Zhang, Y., & Norman, M. L. 1997, New Astronomy, 2, 181, doi: 10.1016/s1384-1076(97)00010-9

Asplund, M., Grevesse, N., Sauval, A. J., & Scott, P. 2009, Annual Review of Astronomy and Astrophysics, 47, 481, doi: 10.1146/annurev.astro.46.060407.145222

Balashev, S. A., Telikova, K. N., & Noterdaeme, P. 2021, Monthly Notices of the Royal Astronomical Society: Letters, 509, L26, doi: 10.1093/mnrasl/slab119

Barthelmy, S. D., Chincarini, G., Burrows, D. N., et al. 2005, Nature, 438, 994, doi: 10.1038/nature04392

Blumenthal, G. R., Faber, S. M., Primack, J. R., & Rees, M. J. 1984, Nature, 311, 517, doi: 10.1038/311517a0

Bothwell, M. S., Maiolino, R., Kennicutt, R., et al. 2013, Monthly Notices of the Royal Astronomical Society, 433, 1425, doi: 10.1093/mnras/stt817

Briggs, F. H. 2005, in The New Cosmology (WORLD SCIENTIFIC), doi: 10.1142/9789812702357_0007

Bromm, V., & Loeb, A. 2006, The Astrophysical Journal, 642, 382, doi: 10.1086/500799

Brown, T., Cortese, L., Catinella, B., & Kilborn, V. 2017, Monthly Notices of the Royal Astronomical Society, 473, 1868, doi: 10.1093/mnras/stx2452

Campana, S., Lazzati, D., Ripamonti, E., et al. 2006, The Astrophysical Journal, 654, L17, doi: 10.1086/510719

Cano, Z., Wang, S.-Q., Dai, Z.-G., & Wu, X.-F. 2017, Advances in Astronomy, 2017, 1, doi: 10.1155/2017/8929054

Christensen, L., Hjorth, J., & Gorosabel, J. 2004, Astronomy &amp Astrophysics, 425, 913, doi: 10.1051/0004-6361:20040361

Chung, A., van Gorkom, J. H., Kenney, J. D. P., Crowl, H., & Vollmer, B. 2009, The Astronomical Journal, 138, 1741, doi: 10.1088/0004-6256/138/6/1741

Cobb, B. E. 2011, Proceedings of the International Astronomical Union, 7, 83, doi: 10.1017/s1743921312012732

Cucchiara, A., Fumagalli, M., Rafelski, M., et al. 2015, The Astrophysical Journal, 804, 51, doi: 10.1088/0004-637x/804/1/51

Curti, M., Mannucci, F., Cresci, G., & Maiolino, R. 2019, Monthly Notices of the Royal Astronomical Society, 491, 944, doi: 10.1093/mnras/stz2910

Dado, S., Dar, A., & De Rujula, A. 2003, doi: 10.48550/ARXIV.ASTRO-PH/0304106

Dickey, J. M., Kulkarni, S. R., Heiles, C. E., & van Gorkom, J. H. 1983, The Astrophysical Journal Supplement Series, 53, 591, doi: 10.1086/190903

Dickey, J. M., Mebold, U., Stanimirovic, S., & Staveley-Smith, L. 2000, The Astrophysical Journal, 536, 756, doi: 10.1086/308953

Dijkstra, M., Haiman, Z., & Loeb, A. 2004, The Astrophysical Journal, 613, 646, doi: 10.1086/422167

Doyle, M. T., & Drinkwater, M. J. 2006, Monthly Notices of the Royal Astronomical Society, 372, 977, doi: 10.1111/j.1365-2966.2006.10931.x

Fall, S. M., & Efstathiou, G. 1980, Monthly Notices of the Royal Astronomical Society, 193, 189, doi: 10.1093/mnras/193.2.189

Fernández, X., Gim, H. B., van Gorkom, J. H., et al. 2016, The Astrophysical Journal, 824, L1, doi: 10.3847/2041-8205/824/1/l1

Field, G. B., Goldsmith, D. W., & Habing, H. J. 1969, The Astrophysical Journal, 155, L149, doi: 10.1086/180324

Field, G. B., & Steigman, G. 1971, The Astrophysical Journal, 166, 59, doi: 10.1086/150941

Floc'h, E. L., Duc, P.-A., Mirabel, I. F., et al. 2003, Astronomy &amp Astrophysics, 400, 499, doi: 10.1051/0004-6361:20030001

Fynbo, J. P. U., Gorosabel, J., Smette, A., et al. 2005, The Astrophysical Journal, 633, 317, doi: 10.1086/432633

Galama, T. J., Vreeswijk, P. M., van Paradijs, J., et al. 1998, Nature, 395, 670, doi: 10.1038/27150

García, T. T. 2006, doi: 10.1111/j.1365-2966.2006.10450.x

Gorosabel, J., Pérez-Ramírez, D., Sollerman, J., et al. 2005, Astronomy &amp Astrophysics, 444, 711, doi: 10.1051/0004-6361:20052768

Heintz, K. E., Watson, D., Oesch, P., Narayanan, D., & Madden, S. C. 2021, doi: 10.3847/1538-4357/ac2231

Hernández-Monteagudo, C., Haiman, Z., Jimenez, R., & Verde, L. 2007, The Astrophysical Journal, 660, L85, doi: 10.1086/518090

Hjorth, J. 2013, Philosophical Transactions of the Royal Society A: Mathematical, Physical and Engineering Sciences, 371, 20120275, doi: 10.1098/rsta.2012.0275

Hjorth, J., & Bloom, J. S. 2011, doi: 10.48550/ARXIV.1104.2274

Hughes, T. M., Cortese, L., Boselli, A., Gavazzi, G., & Davies, J. I. 2013, Astronomy &amp Astrophysics, 550, A115, doi: 10.1051/0004-6361/201218822

Johnson, J. L. 2012, in The First Galaxies (Springer Berlin Heidelberg), 177–222, doi: 10.1007/978-3-642-32362-1_4

Kennicutt, R. C. 1998, Annual Review of Astronomy and Astrophysics, 36, 189, doi: 10.1146/annurev.astro.36.1.189

Kitayama, T., & Yoshida, N. 2005, The Astrophysical Journal, 630, 675, doi: 10.1086/432114

Krogager, J.-K. 2018. https://arxiv.org/abs/1803.01187

Lara-López, M. A., Hopkins, A. M., López-Sánchez, A. R., et al. 2013, Monthly Notices of the Royal Astronomical Society: Letters, 433, L35, doi: 10.1093/mnrasl/slt054

Ledoux, C., Vreeswijk, P. M., Smette, A., et al. 2009, Astronomy &amp Astrophysics, 506, 661, doi: 10.1051/0004-6361/200811572

Leroy, A. K., Walter, F., Brinks, E., et al. 2008, The Astronomical Journal, 136, 2782, doi: 10.1088/0004-6256/136/6/2782

Martin, A. M., Papastergis, E., Giovanelli, R., et al. 2010, The Astrophysical Journal, 723, 1359, doi: 10.1088/0004-637x/723/2/1359

Mihos, J. C., Keating, K. M., Holley-Bockelmann, K., Pisano, D. J., & Kassim, N. E. 2012, The Astrophysical Journal, 761, 186, doi: 10.1088/0004-637x/761/2/186

Mirabel, I. F., & Sanders, D. B. 1988, The Astrophysical Journal, 335, 104, doi: 10.1086/166909

nasa.gov. 2013, Imagine the Universe! — imagine.gsfc.nasa.gov, https://imagine.gsfc.nasa.gov/science/objects/bursts1.html

Noterdaeme, P., Petitjean, P., Ledoux, C., & Srianand, R. 2009, Astronomy &amp Astrophysics, 505, 1087, doi: 10.1051/0004-6361/200912768

Oh, S. P., & Haiman, Z. 2002, The Astrophysical Journal, 569, 558, doi: 10.1086/339393

Prochaska, J. X., Chen, H.-W., Dessauges-Zavadsky, M., & Bloom, J. S. 2007, The Astrophysical Journal, 666, 267, doi: 10.1086/520042

Prochaska, J. X., Bloom, J. S., Chen, H.-W., et al. 2004, The Astrophysical Journal, 611, 200, doi: 10.1086/421988

Prochaska, J. X., Sheffer, Y., Perley, D. A., et al. 2008, The Astrophysical Journal, 691, L27, doi: 10.1088/0004-637x/691/1/l27

Rauch, M., Haehnelt, M., Bunker, A., et al. 2008, The Astrophysical Journal, 681, 856, doi: 10.1086/525846

Read, J. I., Pontzen, A. P., & Viel, M. 2006, Monthly Notices of the Royal Astronomical Society, 371, 885, doi: 10.1111/j.1365-2966.2006.10720.x

Rezzolla, L., Giacomazzo, B., Baiotti, L., et al. 2011, The Astrophysical Journal, 732, L6, doi: 10.1088/2041-8205/732/1/l6

Ruiz, M., Lang, R. N., Paschalidis, V., & Shapiro, S. L. 2016, The Astrophysical Journal, 824, L6, doi: 10.3847/2041-8205/824/1/l6

Savaglio, S. 2006, New Journal of Physics, 8, 195, doi: 10.1088/1367-2630/8/9/195

Savaglio, S., Glazebrook, K., & Borgne, D. L. 2009, The Astrophysical Journal, 691, 182, doi: 10.1088/0004-637x/691/1/182

Spitzer, L. 1998, Physical Processes in the Interstellar Medium (Wiley), doi: 10.1002/9783527617722

Stark, D. V., Masters, K. L., Avila-Reese, V., et al. 2021, Monthly Notices of the Royal Astronomical Society, 503, 1345, doi: 10.1093/mnras/stab566

Tumlinson, J., Peeples, M. S., & Werk, J. K. 2017, Annual Review of Astronomy and Astrophysics, 55, 389, doi: 10.1146/annurev-astro-091916-055240

Vreeswijk, P. M., Ledoux, C., Smette, A., et al. 2007, Astronomy &amp Astrophysics, 468, 83, doi: 10.1051/0004-6361:20066780

Wolfe, A. M., Gawiser, E., & Prochaska, J. X. 2005, Annual Review of Astronomy and Astrophysics, 43, 861, doi: 10.1146/annurev.astro.42.053102.133950

Wolfe, A. M., Prochaska, J. X., & Gawiser, E. 2003, The Astrophysical Journal, 593, 215, doi: 10.1086/376520

Wolfe, A. M., Prochaska, J. X., Jorgenson, R. A., & Rafelski, M. 2008, The Astrophysical Journal, 681, 881, doi: 10.1086/588090

Wolfire, M. G., Hollenbach, D., McKee, C. F., Tielens, A. G. G. M., & Bakes, E. L. O. 1995, The Astrophysical Journal, 443, 152, doi: 10.1086/175510

Wong, O. I., Meurer, G. R., Zheng, Z., et al. 2016, Monthly Notices of the Royal Astronomical Society, 460, 1106, doi: 10.1093/mnras/stw993

Xu, H., Wise, J. H., & Norman, M. L. 2013, The Astrophysical Journal, 773, 83, doi: 10.1088/0004-637x/773/2/83

Zeh, A., A. Kann, D., Klose, S., & H. Hartmann, D. 2005, Il Nuovo Cimento C, 28, 617–620, doi: 10.1393/ncc/i2005-10114-5

Zwaan, M. A., Meyer, M. J., Staveley-Smith, L., & Webster, R. L. 2005, Monthly Notices of the Royal Astronomical Society: Letters, 359, L30, doi: 10.1111/j.1745-3933.2005.00029.x